MATHEMATICAL MODEL FOR BIDIRECTIONAL DC–DC CONVERTER WITHIN BATTERY ELECTRIC VEHICLE SYSTEM USING GENERALIZED STATE SPACE AVERAGING APPROACH

Thitipat Thanrin[1], Jakkrit Pakdeeto[2], Pawin Seesamlee[1], and Kongpan Areerak[1,*]

Received: October 16, 2025; Revised: December 16, 2025; Accepted: January 16, 2026

Abstract

This paper presents the derivation of a mathematical model for a battery electric vehicle (BEV) system in which a bidirectional buck-boost converter is used to regulate the high-voltage DC bus. This converter operates in two modes-step-up (boost) and step-down (buck). The proposed model was developed using the generalized state-space averaging approach, which eliminates time-dependent variables, to obtain a time-invariant model that would accurately represent the averaged dynamic behavior of the system. In addition, a simplified battery model was integrated into the overall dynamic model of the BEV system to enhance accuracy. The proposed model was validated by comparing its responses with those provided by SimPowerSystem simulations in MATLAB/Simulink. The results confirm that the proposed model accurately reproduces both transient and steady-state responses, indicating its effectiveness and suitability for future applications, such as stability analysis, controller design, and performance evaluation under various operating conditions.

Keywords: **Battery electric vehicle; Bidirectional buck–boost converter; Generalized state space averaging method; Mathematical model**

Nomenclature

SOC	State of charge of the battery
V_{OC}	Open-circuit voltage of the battery
$V_{Batt,nom}$	Nominal voltage of the battery
$Q_{Batt,nom}$	Nominal capacity of the battery
L	Inductance of the converter
C	Capacitance of the converter at the HVDC bus side
C_{Batt}	Capacitance of the converter at the battery side
R_{int}	Internal resistance of the battery

[1] *School of Electrical Engineering, Institute of Engineering, Suranaree University of Technology, Nakhon Ratchasima, Thailand. E-mail: best.dankwian@gmail.com; pawinboss44@gmail.com; kongpan@sut.ac.th*[*]
[2] *Department of Teacher Training in Electrical Engineering, Faculty of Technical Education, King Mongkut's University of Technology North Bangkok, Bangkok, Thailand. E-mail: jakkritpa@kmutnb.ac.th*
[*] *Corresponding author*

DOI: https://doi.org/10.55766/sujst11838

d	Duty cycle of the converter
T_s	Switching period of the converter
f_s	Switching frequency of the converter
f_r	Resonant frequency
ω_{nv}	Natural frequency of the voltage loop
ω_{ni}	Natural frequency of the current loop
ζ_v	Damping ratio of the voltage loop
ζ_i	Damping ratio of the current loop
A_r	Peak of the carrier signal
K_{pv}	P-gain of the voltage loop
K_{iv}	I-gain of the voltage loop
K_{pi}	P-gain of the current loop
K_{ii}	I-gain of the current loop
i_{Batt}	Battery current
i_L	Current inductor of the converter
v_H	HVDC bus voltage
v_{Batt}	Battery voltage
Δi_L	Ripple current through L
Δv_C	Ripple voltage across C
$\Delta v_{C_{Batt}}$	Ripple voltage across C_{Batt}

Introduction

In recent years, electric vehicles (EVs) have rapidly advanced worldwide because of the increasing need to reduce dependence on fossil fuels. Fossil fuels are a major contributor to climate change and various environmental issues. The advancement of EV technology also aligns with clean energy policies and environmental protection initiatives put forth by many governments. The global goal of reducing greenhouse gas emissions and mitigating air pollution in urban areas has positioned EVs as a key component of modern, sustainable, and environmentally friendly transportation systems (Gnanavendan *et al.*, 2024; Jiang *et al.*, 2024). Currently, EVs can be classified into several types (Sanguesa *et al.*, 2021; Ehsani *et al.*, 2021), including hybrid EVs, plug-in hybrid EVs, fuel cell EVs, and battery EVs (BEVs). Among these, the BEV powertrain is commonly used to represent other EV configurations because it adopts a fundamental electrical architecture and relies on electricity as the sole energy source.

In terms of electrical architecture, BEVs typically possess a high-voltage DC (HVDC) bus with a voltage of around 800 V (Jung, 2017; Poorfakhraei *et al.*, 2021) to enhance power transmission efficiency, reduce system current, and shorten battery charging time. This configuration improves the overall system efficiency and ensures a faster dynamic response, as shown in Figure 1. The electrical system of a BEV (Figure 1) consists of several major components. The battery pack serves as the primary energy source, supplying power to the traction system and other onboard electrical systems. The bidirectional DC–DC converter boosts the DC voltage from the battery to

a higher bus level suitable for the electric motor drive system. The inverter converts the HVDC bus power into AC power to drive the traction motor. In addition, an auxiliary power converter supplies energy to low-voltage subsystems, including infotainment, lighting, and comfort-supporting equipment. Power converters in BEV systems are typically controlled in closed-loop configurations to regulate voltage levels, particularly in the motor drive stage (Emadi *et al.*, 2006; Khaligh *et al.*, 2008). As the motor drive typically maintains the motor speed constant, it behaves as a constant power load (CPL) with a

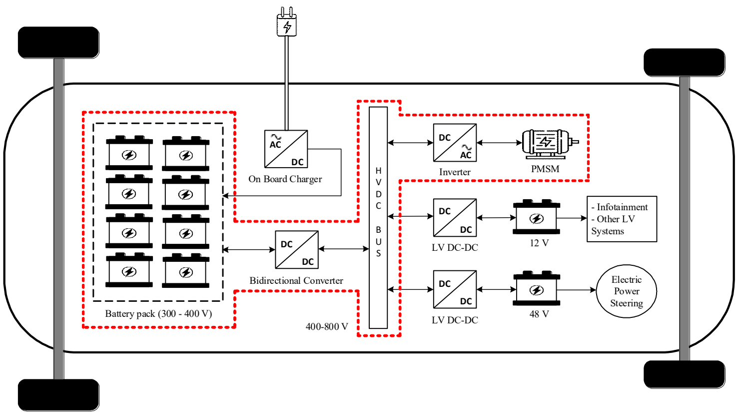

Figure 1. Architecture of a battery electric vehicle

negative impedance (Emadi *et al*., 2006; Areerak *et al*., 2012; Areerak *et al*., 2018).

Previous studies (Emadi *et al*., 2006; Phosung *et al*., 2022) have shown that CPLs considerably affect system stability, which is primarily analyzed through mathematical modeling. Mathematical models are utilized not only for stability analysis but also for controller design and studying system responses under various operating conditions. Therefore, deriving an accurate mathematical model is crucial, as it enables more effective dynamic behavior analysis. Moreover, the use of mathematical models can substantially reduce the simulation time.

Figure 1 shows that the main power conversion component is the bidirectional DC-DC converter. Several types of bidirectional DC-DC converters have been previously developed (Wang *et al*., 2022; Tuluhong *et al*., 2025), including bidirectional Ćuk converters, interleaved bidirectional converters, bidirectional flyback converters, and bidirectional push-pull converters. However, the present study focused on the bidirectional buck–boost converter because of its simple structure and high energy conversion efficiency (Wang *et al*., 2022; Tuluhong *et al*., 2025).

Previous studies (Mahdavi *et al*., 1997) reported that the dynamic models of power converters are generally time-dependent because of internal switching devices, which complicates the analysis of system stability and controller design. However, time-invariant mathematical models have been developed to facilitate system response analysis, controller design, and system stability assessment based on classical control theory. In recent literature, several modeling approaches have been widely adopted, including the harmonic state-space model (HSSM) (Motwani *et al*., 2022) and the dynamic phasor model (DPM) (Shah *et al*., 2021; Lyu *et al*., 2023). Both approaches are inherently complex. The HSSM is based on the concept of linear time-periodic systems and employs Fourier series expansion to characterize the harmonic components of system signals in the frequency domain. In contrast, the DPM is derived from the generalized averaging framework and utilizes phasor-based state variables to eliminate the effects of time-varying switching dynamics. Nevertheless, the dynamic phasor model is difficult to apply to small-signal stability analysis. Both methods suffer from high computational complexity, as their resulting state–space representations are typically high-dimensional. In addition, a positive-sequence model (PSM) has been introduced (Shah *et al*., 2021; Du *et al*., 2024). This approach relies on the assumption of a balanced three-phase system operating at the fundamental frequency, yielding a time-invariant representation. Despite its simplicity, the PSM cannot capture harmonic order and is therefore unsuitable for applications involving DC-DC power converters. Therefore, the present study adopted the generalized state-space averaging (GSSA) approach (Sanders *et al*., 1991; Mahdavi *et al*., 1997; Emadi, 2004) to derive the mathematical model. Mahdavi *et al*. (1997) have shown that the GSSA method employs a zero-order approximation, considering only the DC term while neglecting higher-order harmonics. The GSSA approach effectively eliminates time-dependent terms while maintaining high accuracy because higher-order harmonics do not affect the overall stability of the system (Pakdeeto *et al*., 2018; Pakdeeto *et al*., 2021). In addition, higher-order harmonics do not affect the controller design. Previous studies have confirmed that these harmonics do not substantially impact stability analysis and are typically ignored in advanced controller designs. Therefore, herein, the zero-order GSSA method was adopted to remove time-dependent variables. The derived model simplifies the analysis and reduces the computation time for obtaining system responses. Moreover, the present study employed a simplified battery model integrated into the proposed system model to evaluate the behavior of BEVs under realistic operating conditions. The proposed model also considers the state-of-charge (SOC) of the battery, which is a key feature of the stability study. The accuracy of the proposed model was validated against the simulations using SimPowerSystem blocks in MATLAB/Simulink. The results showed that the model accurately captures both transient and steady-state responses. Furthermore, the computation time of the proposed model is substantially lower than that of the SimPowerSystem simulations. The main contributions of the present study are summarized as follows:

- The derived mathematical model reduces the computation time required to obtain system responses.
- The proposed model, which incorporates the SOC from the simplified battery model, can be used to analyze the future impact of battery dynamics on the overall system performance.

This paper is organized into six parts. Part I presents the background, motivation, and significance of the study, as well as a review of related literature and previous research. Part II describes the considered BEV system. Part III details the derivation of the mathematical model of the electrical system using the GSSA method. Part IV focuses on model validation. Part V compares the computation time required to obtain system responses from the proposed model with that from detailed simulations. Finally, Part VI concludes the study.

Materials and Methods

Considered BEV system

The considered BEV system with a rated power of 380 kW is shown in Figure 2. The critical electrical parameters required for practical hardware design under the worst-case operating conditions are summarized as follows. The maximum current flowing through the inductor is approximately 996 A; therefore, the inductor current rating was conservatively specified as 1000 A. In addition, the maximum voltage across the capacitor on the side of the HVDC bus, under transient overshoot conditions, is approximately 850 V. Accordingly, the capacitor voltage rating was selected as 1000 V. Similarly, the voltage rating of the capacitor on the battery side was specified as 1000 V because the battery-side voltage is inherently lower than that of the HVDC bus under normal operating conditions.

The system consists of the following three main parts. The first part is the battery pack, which serves as the main power source, providing a nominal voltage of 569 V and a capacity of 155 Ah. The second part is the bidirectional DC–DC converter, controlled by a cascaded proportional-integral (PI)controller to regulate the HVDC bus voltage. In the present study, a buck-boost converter with two power electronic switches operating alternately was employed. The converter also includes an inductor and a DC filter capacitor to reduce current and voltage ripples. It can operate in two main modes (Tuluhong *et al.*, 2025): in the boost mode, the converter steps up the battery voltage to the HVDC bus during driving conditions, and in the buck mode, it returns regenerative braking energy back to the battery. However, herein, we primarily focused on the boost mode, as it plays an important role in system stability for future analysis. The third part is the load or "motor drive system," which includes a speed controller represented by an ideal CPL. Low-voltage loads at 12 and 48 V were neglected because their effects on the overall system are smaller than the traction motor drive load.

The converter parameters (L and C) depend on the ripple current (Δi_L) and the voltage ripple (Δv_C) (Erickson & Maksimović, 2001). These parameters can be calculated using Equations (1)-(2). In addition, C_{Batt} represents the battery-side capacitor used to reduce the battery voltage ripple, which can be determined using Equation (3).

$$L = \frac{dT_s V_{Batt,nom}}{2\Delta i_L} \tag{1}$$

$$C = \frac{dT_s V_{Batt,nom}}{2\Delta v_C R(1-d)} \tag{2}$$

$$C_{Batt} = \frac{T_s \Delta i_L}{4\Delta v_{C_{Batt}}} \tag{3}$$

where T_s is the switching period of the converter, defined as $1/f_s$ where f_s is the switching frequency of the converter; d is the duty cycle; $V_{Batt,nom}$ is the nominal battery voltage; and R is the

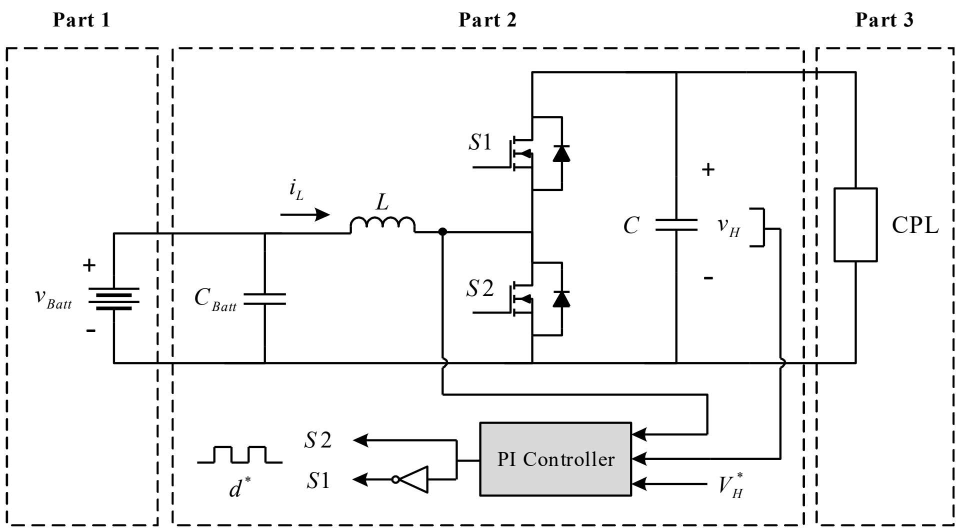

Figure 2. Scheme of the considered BEV system

equivalent resistance corresponding to the CPL, which can be calculated as $R = V_H^2 / P_{CPL}$.

The control system employed in the considered BEV configuration is a cascaded PI controller. It consists of two main control loops: a voltage control loop that regulates the HVDC bus voltage and a current control loop that controls the inductor current. The parameters of the PI controller for both loops were designed by comparing the coefficients of the closed-loop transfer function with those of a standard second-order system (Beraki *et al*., 2017; Pakdeeto *et al*., 2024). The operation of the PI controllers in both the voltage and current loops is governed by Equations (4)–(7).

$$K_{pv} = 2\zeta_v \omega_{nv} C \tag{4}$$

$$K_{iv} = \omega_{nv}^2 C \tag{5}$$

$$K_{pi} = \frac{2\zeta_i \omega_{ni} A_r L}{V_{Batt,nom}} \tag{6}$$

$$K_{ii} = \frac{\omega_{ni}^2 A_r L}{V_{Batt,nom}} \tag{7}$$

where K_{pv} and K_{iv} are the proportional and integral gains of the voltage control loop; ω_{nv} is the natural frequency of the voltage loop; and ζ_v is the damping ratio of the voltage loop. Similarly, K_{pi} and K_{ii} denote the proportional and integral gains of the current control loop; ω_{ni} is the natural frequency of the current loop; ζ_i is the damping ratio of the current loop; and A_r is the peak value of the triangular carrier signal.

Derivation of the Mathematical Model

Herein, the mathematical model was derived using the GSSA approach under the zero-order approximation. In this method, the state variables are expressed as coefficients of the complex Fourier series (Gamelin, 2001). This approach eliminates time-dependent variables, yielding a time-invariant mathematical model. In addition, a simplified battery model was incorporated to enhance the accuracy of the proposed mathematical model. The model derivation assumes that the bidirectional buck–boost converter operates only in continuous conduction mode. The derivation of the mathematical model for the considered electrical system is presented below.

A. Battery model: The battery plays a crucial role in EVs. Therefore, the analysis of battery dynamics is essential. Herein, the battery model was incorporated as a part of the proposed mathematical model. Generally, the behavior of a battery changes over time and can be evaluated by the decrease in its SOC when supplying energy to the load. Tremblay & Dessaint (2009) reported that the realistic characteristic of a battery is defined by the relationship between the terminal voltage (V) and the extracted capacity (Q, in Ah). However, the objective of the present study was to derive a simplified battery model that is independent of time variation and suitable for future stability analysis. Hence, a simplified *V–I* curve independent of time was adopted to determine the operating point of the system because an ideal voltage source cannot reflect the effect of SOC. A simplified battery model (Susanna *et al*., 2019) was employed to improve the accuracy of the overall mathematical model, as shown in Figure 3. This simplified battery model relies on a linear approximation.

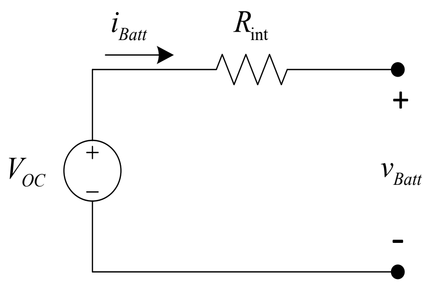

Figure 3. Simplified battery model

As shown in Figure 3, the battery voltage can be calculated using Equation (8), where v_{Batt} is the battery voltage, i_{Batt} is the battery current, V_{OC} is the open-circuit voltage of the battery, and R_{int} is the internal resistance of the battery.

$$v_{Batt} = V_{OC} - i_{Batt} R_{int} \tag{8}$$

The values of V_{OC} and R_{int} were obtained by comparing the linear equation derived through curve fitting with the results of the battery discharge simulation. Herein, the case where the SOC equals 97% was considered in the following procedure.

Step 1: The *V–I* curve was obtained from the battery simulation while the battery supplied power to the load. The battery block was connected to an ideal CPL, and the load power was gradually increased up to the rated value of 380 kW. In this simulation, the nominal battery parameters were $V_{Batt,nom} = 569$ V and $SOC = 97\%$.

Step 2: The obtained *V–I* curve was fitted with a linear equation to obtain a simplified battery model that accurately represents the approximated battery behavior at $SOC = 97\%$, as shown in Figure 4.

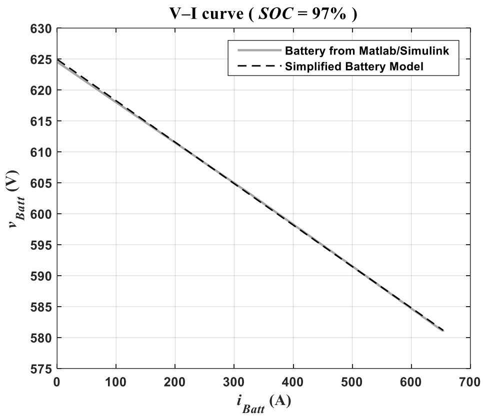

Figure 4. Curve fitting for the simplified battery model

In Figure 4, the dashed line is the *V–I* curve of the simplified battery model, obtained by fitting a linear equation with a slope of –0.0669 and a *y*-intercept of 624.947. The corresponding linear equation is given in (9).

$$y = -0.0669x + 624.947 \tag{9}$$

Step 3: The coefficients in Equations (8) and (9) were compared for the case where $SOC = 97\%$, yielding $V_{OC} = 624.947$ V and $R_{\text{int}} = 0.0669\ \Omega$. However, the validity of the battery model is limited to the SOC range of 14%–97% because the battery behavior outside this range becomes highly nonlinear. Within this SOC range, the converter duty cycle was found to operate between 0.275 and 0.509 under worst-case operating conditions. Therefore, the present study considered only the specified SOC range to ensure modeling accuracy.

B. Ideal CPL model: This section discusses the ideal CPL, which accurately reflects the system behavior under varying load power conditions at each operating point. The ideal CPL is represented by a controlled DC source, as shown in Figure 5 (Rivetta *et al*., 2006; Solsona *et al*., 2015). The current of this power source is defined as $i_{CPL} = P_{CPL} / v_H$, where P_{CPL} is the CPL.

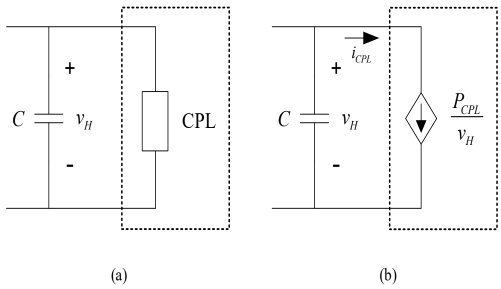

Figure 5. Ideal CPL model

After applying the battery and ideal CPL models to the considered BEV system, the equivalent circuit under open-loop control is shown in Figure 6.

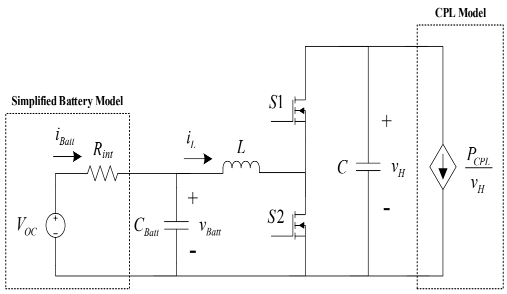

Figure 6. Bidirectional DC–DC converter (open-loop control)

C. Bidirectional DC-DC converter: To elucidate the operating principles of the bidirectional buck–boost converter, its operation was divided into two switching modes. In the first mode, switch $S1$ is off, and switch $S2$ is on. In the second mode, switch $S1$ is on, and switch $S2$ is off. The converter operation in each mode was analyzed (Figure 7) by applying Kirchhoff's laws to derive the differential equations of the state variables involved in the switching states. This representation is referred to as a switched model, which serves as the GSSA model. The state variables of the system can be defined as $\mathrm{X}=\left[i_L\ v_H\ v_{Batt}\right]^T$.

The circuit analysis in Figure 7 provides a switched model that describes the relationship between the derivatives of i_L, v_H, v_{Batt}, and the switching function $u(t)$, as expressed in Equation (10).

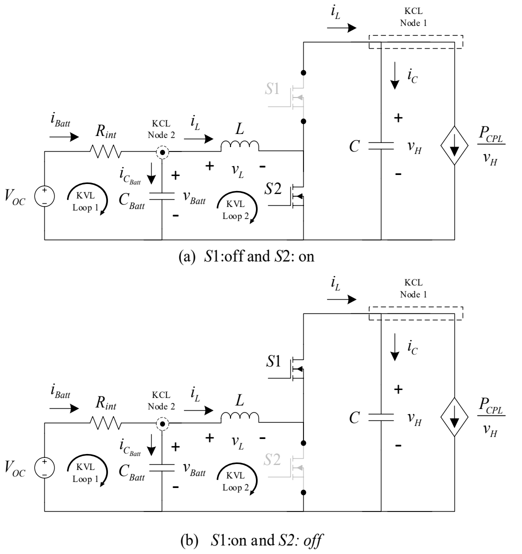

Figure 7. Operating modes of the bidirectional DC–DC converter

$$\begin{cases} \dot{i}_L = \dfrac{1}{L} v_{Batt} - \dfrac{1}{L}(1-u(t)) \cdot v_H \\ \dot{v}_H = \dfrac{1}{C}(1-u(t)) \cdot i_L - \dfrac{P_{CPL}}{v_H C} \\ \dot{v}_{Batt} = \left(\dfrac{V_{OC} - v_{Batt}}{R_{\text{int}} C_{Batt}} \right) - \dfrac{1}{C_{Batt}} i_L \end{cases} \tag{10}$$

After the switched model in Equation (10) was obtained, the GSSA method based on the consideration of a periodic signal $f(t)$ with a period time (T_s) was applied. The periodic function can be expressed as a complex Fourier series (Equation (11)), where $\omega = 2\pi / T_s$ and $\langle x \rangle_k (t)$ are the complex Fourier coefficients of the state variables to be determined, as calculated in Equation (12).

$$f(t) = \sum_{k=-\infty}^{\infty} \langle x \rangle_k e^{jk\omega t} \tag{11}$$

$$\langle x \rangle_k (t) = \frac{1}{T} \int_{1-T}^{t} f(t) e^{-jk\omega t} dt \tag{12}$$

To analyze the switching function of the bidirectional buck–boost converter, the switching pattern was represented as shown in Figure 8 and mathematically expressed in Equation (13). After the application of GSSA, the complex Fourier coefficients of the switching function were obtained from Equation (13) at $k = 0$, as shown in (14). The d value was then calculated as t_{on} / T_s.

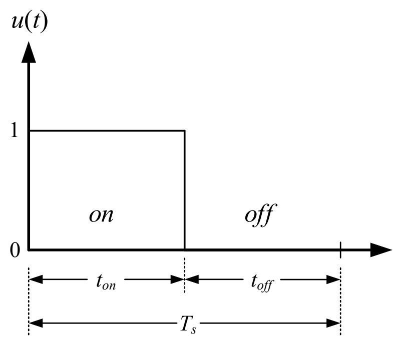

Figure 8. Switching function of the bidirectional DC–DC converter

$$u(t) = \begin{cases} 1, & 0 < t < dT_s \\ 0, & dT_s < t < T_s \end{cases} \tag{13}$$

$$\langle u \rangle_0 (t) = \frac{1}{T_s} \int_0^{dT_s} u(t) e^0 dt = \frac{dT_s}{T_s} = d \tag{14}$$

To derive the state variables using the GSSA method, two properties of the complex Fourier series described in (Sanders *et al.*, 1991; Wang *et al.*, 2019) were applied as follows:

- The properties of the time-derivative are shown in (15).

$$\frac{d}{dt} \langle x \rangle_k = \left\langle \frac{dx}{dt} \right\rangle_k - jk\omega \langle x \rangle_k \tag{15}$$

- The properties of multiplication are shown in (16).

$$\langle xy \rangle_k = \sum_i \langle x \rangle_{k-i} \langle y \rangle_i \tag{16}$$

If k is set to 0, the model excludes high-frequency components but can still accurately represent the dynamic behavior of the system. As for the switched model in Equation (10), i_L, v_H and v_{Batt} can be expressed in terms of complex Fourier coefficients, as shown in Equation (17), where $\langle i_L \rangle_0$, $\langle v_H \rangle_0$ and $\langle v_{Batt} \rangle_0$ are defined as the state variables of the model in Equation (18).

$$\begin{cases} i_L = \langle i_L \rangle_0 = x_1 \\ v_H = \langle v_H \rangle_0 = x_2 \\ v_{Batt} = \langle v_{Batt} \rangle_0 = x_3 \end{cases} \tag{17}$$

$$\begin{cases} \langle \dot{i}_L \rangle_0 = \dfrac{1}{L} v_{Batt} - \dfrac{\left(1-\langle u \rangle_0 (t)\right)}{L} \cdot \langle v_H \rangle_0 \\ \langle \dot{v}_H \rangle_0 = \dfrac{\left(1-\langle u \rangle_0 (t)\right)}{C} \cdot \langle i_L \rangle_0 - \dfrac{P_{CPL}}{\langle v_H \rangle_0 C} \\ \langle \dot{v}_{Batt} \rangle_0 = \left(\dfrac{V_{OC} - \langle v_{Batt} \rangle_0}{R_{\text{int}} C_{Batt}} \right) - \dfrac{1}{C_{Batt}} \cdot \langle i_L \rangle_0 \end{cases} \tag{18}$$

After $\langle u \rangle_0 (t)$ from Equation (14) is substituted into Equation (18), and the multiplication property from (16) is applied, the mathematical model of the bidirectional buck–boost power converter (open-loop control) becomes Equation (19) using the GSSA method under the zero-order approximation.

HVDC bus; and i_L^* is the reference current flowing through the inductor. In addition, d^* can be expressed as shown in Equation (22).

$$\dot{x}_v = v_H^* - v_H \tag{20}$$

$$\dot{x}_i = i_L^* - i_L \tag{21}$$

$$\begin{aligned} d^* = \frac{1}{A_r} (&K_{pi} K_{pv} v_H^* - K_{pi} K_{pv} v_H \\ &+ K_{pi} K_{iv} x_v - K_{pi} i_L + K_{ii} x_i) \end{aligned} \tag{22}$$

E. Considered system mathematical model: The dynamic model of the considered system was obtained by integrating the simplified battery model, ideal CPL model, open-loop bidirectional DC–DC converter, and cascade PI controller. However, d in Equation (19) was substituted by d^* from Equation (22). The complete dynamic model of the proposed BEV system is presented in Equation (23).

The proposed model in Equation (23)

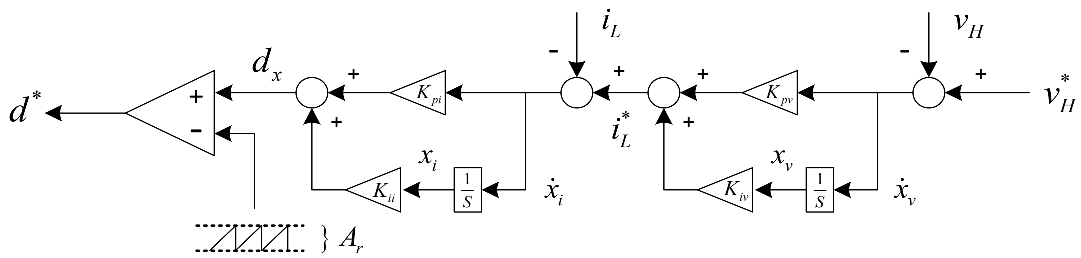

Figure 9. Cascade PI controller

$$\begin{cases} \dot{x}_1 = -\dfrac{(1-d)}{L} \cdot x_2 + \dfrac{1}{L} \cdot x_3 \\ \dot{x}_2 = \dfrac{(1-d)}{C} \cdot x_1 - \dfrac{P_{CPL}}{x_2 C} \\ \dot{x}_3 = \left(\dfrac{V_{OC} - x_3}{R_{\text{int}} C_{Batt}} \right) - \dfrac{1}{C_{Batt}} \cdot x_1 \end{cases} \tag{19}$$

D. Cascade PI controller: The cascade PI controller structurally consists of voltage and current loops (Figure 9). From Figure 9, x_v and x_i are the state variables of the voltage and current control loops, as shown in Equations (20) and (21), respectively; v_H^* is the reference voltage of the

represents the mathematical model of the considered BEV system derived using the GSSA method under the zero-order approximation. However, the mathematical model in Equation (23) is nonlinear. To enable the use of this model as a tool for future stability analysis based on linear control theory, a linearized model was derived using a first-order Taylor series expansion (Daengdon *et al.*, 2025), which provides a local approximation around the system operating point. The resulting linearized equations can be expressed in the state-space form of a small-signal model, as given in Equation (24). The detailed expressions of the system Jacobian matrices $\mathbf{A}(x_0,u_0)$ $\mathbf{B}(x_0,u_0)$, $\mathbf{C}(x_0,u_0)$, and $\mathbf{D}(x_0,u_0)$ are provided in the Appendix.

$$\begin{cases}\dot{x}_1 = -\dfrac{1}{L}x_2 + \dfrac{K_{pi}K_{pv}}{A_r L}x_2 x_2^* - \dfrac{K_{pi}K_{pv}}{A_r L}x_2^2 + \dfrac{K_{pi}K_{iv}}{A_r L}x_v x_2 - \dfrac{K_{pi}}{A_r L}x_1 x_2 + \dfrac{K_{ii}}{A_r L}x_i x_2 + \dfrac{1}{L}\cdot x_3 \\ \dot{x}_2 = \dfrac{1}{C}x_1 - \dfrac{K_{pi}K_{pv}}{A_r C}x_1 x_2^* + \dfrac{K_{pi}K_{pv}}{A_r C}x_1 x_2 - \dfrac{K_{pi}K_{iv}}{A_r C}x_v x_1 + \dfrac{K_{pi}}{A_r C}x_1^2 - \dfrac{K_{ii}}{A_r C}x_i x_1 - \dfrac{P_{CPL}}{x_2 C} \\ \dot{x}_3 = \dfrac{V_{OC}}{R_{\text{int}}C_{Batt}} - \dfrac{1}{R_{\text{int}}C_{Batt}}x_3 - \dfrac{1}{C_{Batt}}x_1 \\ \dot{x}_v = x_2^* - x_2 \\ \dot{x}_i = -x_1 - K_{pv}x_2 + K_{iv}x_v + K_{pv}x_2^* \end{cases} \tag{23}$$

$$\begin{cases}\delta\dot{\mathbf{x}} = \mathbf{A}(\mathrm{x}_0,\mathrm{u}_0)\delta\mathbf{x} + \mathbf{B}(\mathrm{x}_0,\mathrm{u}_0)\delta\mathbf{u} \\ \delta\mathbf{y} = \mathbf{C}(\mathrm{x}_0,\mathrm{u}_0)\delta\mathbf{x} + \mathbf{D}(\mathrm{x}_0,\mathrm{u}_0)\delta\mathbf{u}\end{cases} \tag{24}$$

State-space variables:
$\delta\mathbf{x} = \left[\delta x_1\ \delta x_2\ \delta x_3\ \delta x_v\ \delta x_i\right]^T$

Input variables: $\delta\mathbf{u} = \left[\delta x_2^*\ \delta P_{CPL}\ \delta V_{OC}\right]^T$ Output variables: $\delta\mathbf{y} = \left[\delta x_1\ \delta x_2\ \delta x_3\right]^T$

Results and Discussion

Model Validation

To confirm the accuracy of the mathematical model expressed in Equation (23), the dynamical responses from the proposed model were compared with the simulation responses from a power system block in MATLAB/SIMULINK. The system parameters are listed in Table 1. For model validation, the voltage of the HVDC bus was regulated at 800 V, and the ideal CPL was changed from 290 to 300 kW, with the SOC value varied at 97%, 60%, and 35%. The system responses of i_L, v_H, and v_{Batt} are shown in Figures 10-12, respectively. In addition, for the buck mode, the system response at $SOC = 60\%$ is provided in Figure 13.

The simulation results (Figures 10-13) verify that the proposed mathematical model of the BEV system in both boost and buck modes, derived using the GSSA method under the zero-order approximation, is highly accurate. However, the present study primarily analyzed the boost operating mode, as it directly affects the stability of the BEV system and is an important topic for future research. The simplified battery model used herein was formulated based only on the boost mode. As a result, the accuracy of the model in the buck mode is limited to the SOC range of 40%-60%. To improve the accuracy of the model in the buck mode, the *V-I* characteristic of the simplified battery model in the buck mode can be further considered in future work.

Table 1. System parameters

Symbol	Descriptions	Values
$V_{Batt,nom}$	Nominal Battery Voltage	569 V
$Q_{Batt,nom}$	Nominal Battery Capacity	155 Ah
C_{Batt}	Capacitance (Battery Side) of the Converter	19.846 µF
C	Capacitance (HVDC Bus Side) of the Converter	2.287 mF
L	Inductance of the Converter	3.45 mH
f_s	Switching frequency of the converter	10 kHz
ω_{nv}	Natural frequency of the voltage loop	2π ×27 rad/s
ω_{ni}	Natural frequency of the current loop	2π×300 rad/s
ζ_v	Damping ratio of the voltage loop	0.95
ζ_i	Damping ratio of the voltage loop	0.85
A_r	Peak of the Triangular Wave Form	10
K_{pv}	Parameter of the Voltage Loop P-Controller	0.73718
K_{iv}	Parameter of the Voltage Loop I-Controller	65.8224
K_{pi}	Parameter of the Current Loop P-Controller	0.19430
K_{ii}	Parameter of the Current Loop I-Controller	215.442

As shown in Figures 10-13, the proposed model responses closely match those obtained from MATLAB/Simulink simulations under both transient and steady-state conditions. The errors of v_H in these figures are negligible and approximately zero. When the load power changes from 290 to 300 kW in the boost mode and from 10 to -10 kW in the buck mode, the PI controller effectively maintains the HVDC bus voltage at 800 V, even as the SOC

of the battery decreases. Moreover, the spectral analysis of v_H in Figures 10-13 shows an amplitude of approximately 10 kHz, which corresponds to the switching frequency of the power converter. Another frequency component appears in the range of 180–200 Hz, which was attributed to the zero-order approximation used in the GSSA method. Nevertheless, these frequency components do not affect the stability analysis of the system or the controller design. This is because the frequencies in this range do not coincide with the resonance frequency of the system, which is approximately 56.66 Hz and represents the dominant frequency. The resonance frequency can be calculated using Equation (25) (Li, 2009).

$$f_r = \frac{1}{2\pi\sqrt{LC}} \approx 56.66 \text{ Hz} \tag{25}$$

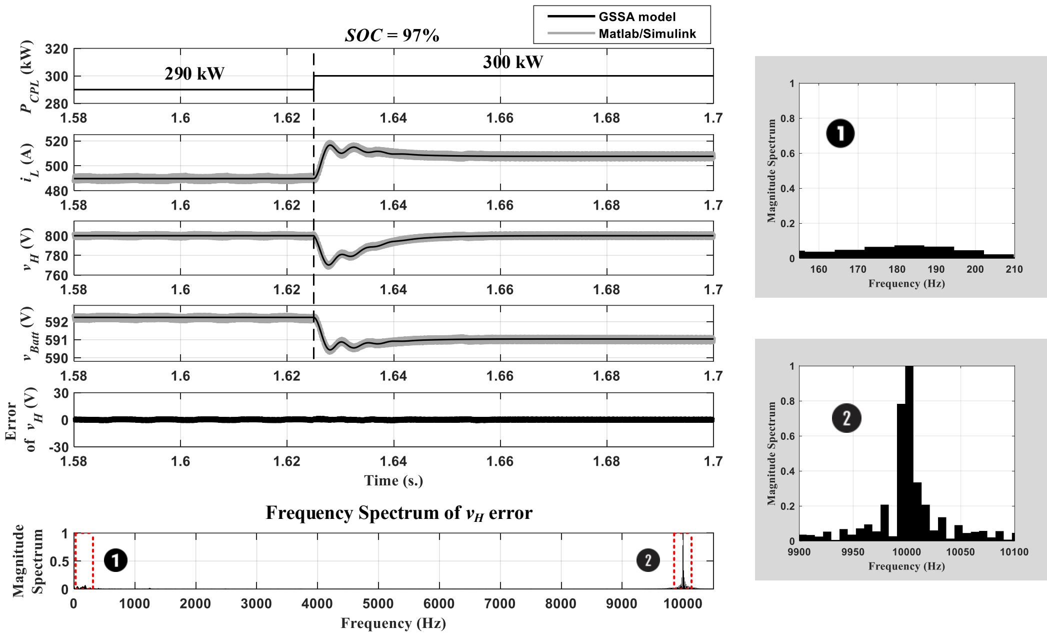

Figure 10. **System responses in the boost mode at a *SOC* of 97%**

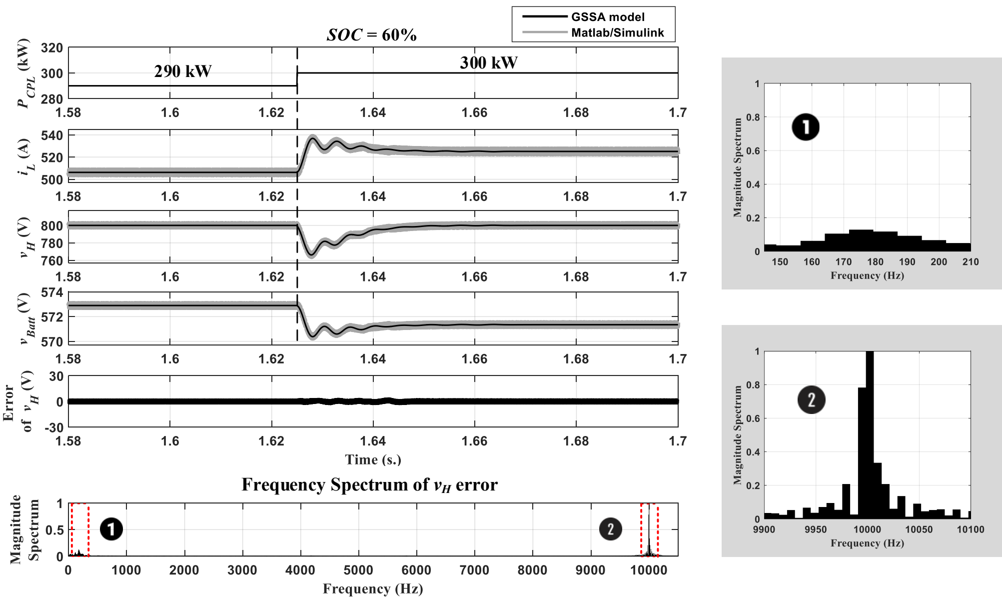

Figure 11. **System responses in the boost mode at a *SOC* of 60%**

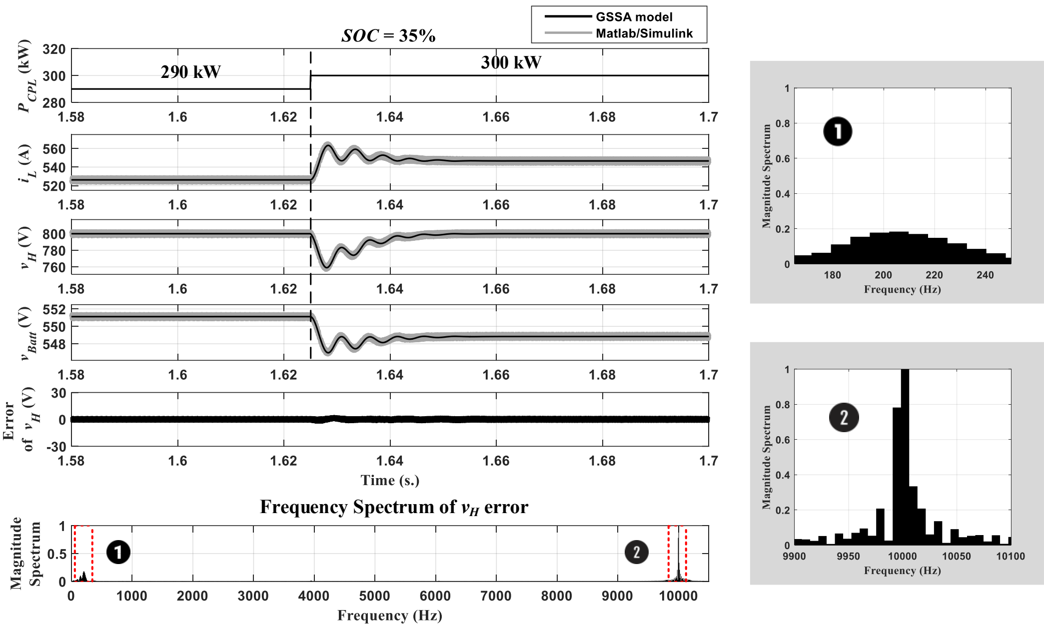

Figure 12. System responses in the boost mode at a *SOC* of 35%

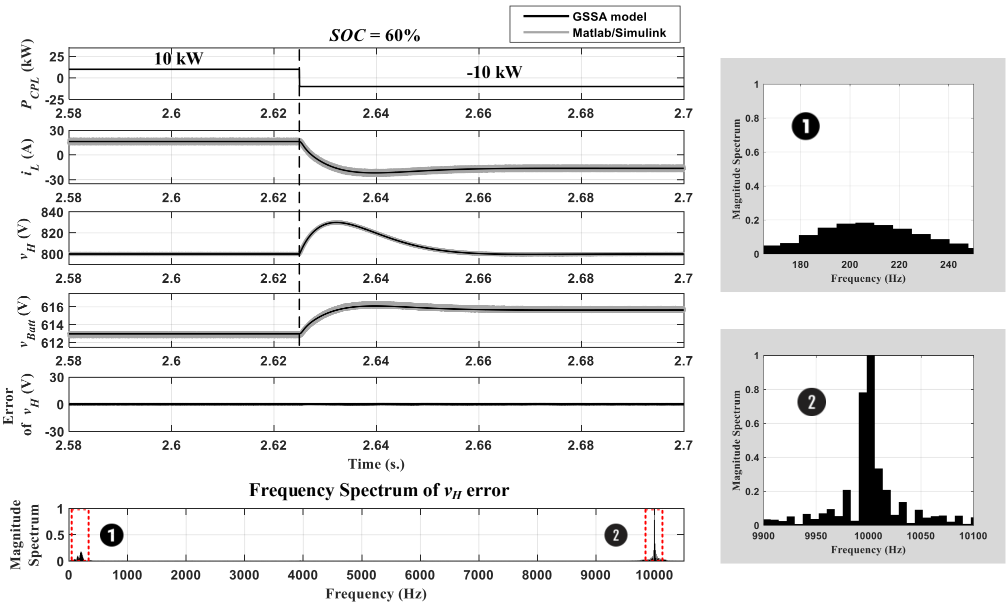

Figure 13. System responses in the buck mode at a *SOC* of 60%

Time Saving

The validated mathematical model developed herein is not only accurate and suitable for future applications but also considerably faster to compute. To compare the performance of the proposed model with that of the MATLAB/Simulink power block simulation, these two simulations were conducted on a computer equipped with an Intel(R) Core(TM) i5-9300H CPU (2.40 GHz), 16 GB RAM, and Windows 11 (64-bit) operating system using MATLAB R2022a. The comparison of simulation times is presented in Table 2, and the percentage of time reduction was calculated using Equation (26), where t_{exact} is the time required for simulation using MATLAB/Simulink, and t_{math} is the time required to obtain the response from the proposed mathematical model.

Table 2. Comparison of the simulation time

Operating mode	*SOC* (%)	Exact model (s)	GSSA model (s)	Time saving (%)
Boost	97	64.230	9.241	85.613
	60	64.502	9.937	84.594
	35	73.368	10.227	86.061
Buck	60	145.474	11.509	92.089
Average		86.894	10.228	87.089

$$\%t_{saving} = \frac{t_{exact} - t_{math}}{t_{exact}} \times 100\% \tag{26}$$

Table 2 indicates that the proposed mathematical model offers 87.089% lower computation time, indicating its excellent computational efficiency while maintaining response accuracy. Therefore, the model derived herein is an effective tool for future studies, including stability analysis, parameter sensitivity investigation, and controller design.

Conclusion

The proposed study presents a mathematical model for a BEV system operated with an internal bidirectional buck-boost power converter. This converter can operate in both buck and boost modes. The proposed model was derived using the GSSA method under a zero-order approximation to eliminate the time variable. In addition, a simplified battery model was employed to represent the effect of SOC and to improve model accuracy. However, the proposed model is valid only when the power converter operates in the continuous conduction mode. The main advantage of the proposed model is its ability to substantially reduce the computation time required to obtain system responses. The proposed mathematical model was validated against the MATLAB/Simulink simulation. The results confirmed that the proposed model accurately provides both transient and steady-state responses, making it suitable for future applications, such as stability analysis and controller design. Moreover, the GSSA model requires an average simulation time of only 10.228 s, whereas the exact topological model implemented in MATLAB/Simulink requires 86.894 s. As a result, the GSSA model reduces computation time by approximately 87.089% compared with the exact topological model.

Acknowledgement

Kongpan Areerak would like to acknowledge Suranaree University of Technology (SUT) for research funding. Jakkrit Pakdeeto appreciates the support from the King Mongkut's University of Technology North Bangkok (KMUTNB) Contract No. FTE-2568-09.

References

Areerak, K.-N., Bozhko, S., Asher, G. M., De Lillo, L., & Thomas, D. W. P. (2012). Stability study for a hybrid AC–DC more-electric aircraft power system. *IEEE Transactions on Aerospace and Electronic Systems*, *48*(1), 329-347. https://doi.org/10.1109/TAES.2012.6129630

Areerak, K.-N., Sopapirm, T., Bozhko, S., Hill, C. I., Suyapan, A., & Areerak, K.-L. (2018). Adaptive stabilization of uncontrolled rectifier-based AC–DC power systems feeding constant power loads. *IEEE Transactions on Power Electronics*, *33*(10), 8927-8935. https://doi.org/10.1109/TPEL.2017.2774826

Beraki, M. W., Trovão, J. P. F., Perdigão, M. S., & Dubois, M. R. (2017). Variable inductor-based bidirectional DC-DC converter for electric vehicles. *IEEE Transactions on Vehicular Technology*, *66*(10), 8764-8772. https://doi.org/10.1109/TVT.2017.2711818

Daengdon, S., Suyapan, A., Areerak, K.-N., & Pakdeeto, J. (2025). Stability investigation of an AC-DC power system feeding a buck converter controlled by sliding mode controller. *IEEE Access*, *13*, 116234-116245. https://doi.org/10.1109/ACCESS.2025.3585767

Du, W., Nguyen, Q. H., Wang, S., Kim, J., Liu, Y., & Zhu, S. (2024). Positive-sequence modeling of droop-controlled grid-forming inverters for transient stability simulation of transmission systems. *IEEE Transactions on Power Delivery*, *39*(3), 1736-1748. https://doi.org/10.1109/TPWRD.2024.3376245

Ehsani, M., Singh, K. V., Bansal, H. O., & Mehrjardi, R. T. (2021). State of the art and trends in electric and hybrid electric vehicles. *Proceedings of the IEEE*, *109*(6), 967-984. https://doi.org/10.1109/JPROC.2021.3060484

Emadi, A. (2004). Modeling and analysis of multiconverter DC power electronic systems using the generalized state-space averaging method. *IEEE Transactions on Industrial Electronics*, *51*(3), 661-668. https://doi.org/10.1109/TIE.2004.825345

Emadi, A., Khaligh, A., Rivetta, C. H., & Williamson, G. A. (2006). Constant power loads and negative impedance instability in automotive systems: Definition, modeling, stability, and control of power electronic converters and motor drives. *IEEE Transactions on Vehicular Technology*, *55*(4), 1112-1125. https://doi.org/10.1109/TVT.2006.877480

Erickson, R. W., & Maksimović, D. (2001). *Fundamentals of power electronics*. Kluwer Academic Publishers.

Gamelin, T. W. (2001). *Complex analysis*. Springer.

Gnanavendan, S., Selvaraj, S. K., Dev, S. J., Mahato, K. K., Swathish, R. S., & Sundaramali, G. (2024). Challenges, solutions, and future trends in EV-technology: A review.

IEEE Access, *12*, 17242-17260. https://doi.org/10.1109/ACCESS.2024.3350000

Jiang, B.-H., Hsu, C.-C., Su, N.-W., & Lin, C.-C. (2024). A review of modern electric vehicle innovations for energy transition. *Energies*, *17*(12), 2906. https://doi.org/10.3390/en17122906

Jung, C. (2017). Power up with 800-V systems: The benefits of upgrading voltage power for battery-electric passenger vehicles. *IEEE Electrification Magazine*, *5*(1), 53-58. https://doi.org/10.1109/MELE.2017.2666440

Khaligh, A., Rahimi, M., & Emadi, A. (2008). Modified pulse-adjustment technique to control DC/DC converters driving variable constant-power loads. *IEEE Transactions on Industrial Electronics*, *55*(3), 1133-1146. https://doi.org/10.1109/TIE.2007.911946

Li, Y. W. (2009). Control and resonance damping of voltage-source and current-source converters with LC filters. *IEEE Transactions on Industrial Electronics*, *56*(5), 1511-1521. https://doi.org/10.1109/TIE.2008.2009562

Lyu, X., Wang, X., Che, Y., & Li, L. (2023). Dynamic phasor modeling and low-frequency oscillation analysis of single-phase vehicle-grid system. *CSEE Journal of Power and Energy Systems*, *9*(1), 158-171. https://doi.org/10.17775/CSEEJPES.2020.03160

Mahdavi, J., Emadi, A., Bellar, M. D., & Ehsani, M. (1997). Analysis of power electronic converters using the generalized state-space averaging approach. *IEEE Transactions on Circuits and Systems I: Fundamental Theory and Applications*, *44*(8), 767-770. https://doi.org/10.1109/81.611257

Motwani, J. K., Xue, Y., Nazari, A., Dong, D., Cvetkovic, I., & Boroyevich, D. (2022). Modeling of power electronics systems and PWM modulators in harmonic-state space. *IEEE Open Journal of Power Electronics*, *3*, 689-704. https://doi.org/10.1109/OJPEL.2022.3205893

Pakdeeto, J., Areerak, K.-N., & Areerak, K.-L. (2018). Modelling and stability analysis of AC–DC power systems feeding a speed controlled DC motor. *Journal of Electrical Engineering & Technology*, *13*(4), 1566-1577. https://doi.org/10.5370/JEET.2018.13.4.1566

Pakdeeto, J., Thanommuang, A., Chaicharoenudomrung, K., Areerak, K., & Areerak, K. (2021). The effect of parameter variations of system stability for AC–DC power system feeding controlled buck converter. In *2021 International Conference on Power, Energy and Innovations (ICPEI)* (pp. 524-527). IEEE. https://doi.org/10.1109/ICPEI52436.2021.9690662

Pakdeeto, J., Thanommuang, A., & Areerak, K. (2024). The DC voltage controller design of traction substation in heavy rail systems. In *2024 12th International Electrical Engineering Congress (iEECON)*. IEEE. https://doi.org/10.1109/IEECON60677.2024.10537888

Phosung, R., Areerak, K.-N., Sopapirm, T., & Areerak, K.-L. (2022). Design and optimization of instability mitigation for AC–DC feeder systems with constant power loads using artificial intelligence techniques. *IEEE Transactions on Power Electronics*, *37*(5), 5385-5397. https://doi.org/10.1109/TPEL.2021.3120673

Poorfakhraei, A., Narimani, M., & Emadi, A. (2021). A review of multilevel inverter topologies in electric vehicles: Current status and future trends. *IEEE Open Journal of Power Electronics*, *2*, 155-170. https://doi.org/10.1109/OJPEL.2021.3066509

Rivetta, C. H., Emadi, A., Williamson, G. A., Jayabalan, R., & Fahimi, B. (2006). Analysis and control of a buck DC-DC converter operating with constant power load in sea and undersea vehicles. *IEEE Transactions on Industry Applications*, *42*(2), 559-572. https://doi.org/10.1109/TIA.2006.870095

Sanders, S. R., Noworolski, J. M., Liu, X. Z., & Verghese, G. C. (1991). Generalized averaging method for power conversion circuits. *IEEE Transactions on Power Electronics*, *6*(2), 251-259. https://doi.org/10.1109/63.76811

Sanguesa, J. A., Torres-Sanz, V., Garrido, P., Martinez, F. J., & Marquez-Barja, J. M. (2021). A review on electric vehicles: Technologies and challenges. *Smart Cities*, *4*(1), 372-404. https://doi.org/10.3390/smartcities4010022

Shah, C., Vasquez-Plaza, J. D., Campo-Ossa, D. D., Patarroyo-Montenegro, J. F., Guruwacharya, N., Bhujel, N., Trevizan, R. D., Rengifo, F. A., Shirazi, M., Tonkoski, R., Hansen, T. M., Wies, R., & Cicilio, P. (2021). Review of dynamic and transient modeling of power electronic converters for converter dominated power systems. *IEEE Access*, *9*, 82094-82117. https://doi.org/10.1109/ACCESS.2021.3086420

Solsona, J. A., Jorge, S. G., & Busada, C. A. (2015). Nonlinear control of a buck converter which feeds a constant power load. *IEEE Transactions on Power Electronics*, *30*(12), 7193-7201. https://doi.org/10.1109/TPEL.2015.2388781

Susanna, S., Dewangga, B. R., Wahyungoro, O., & Cahyadi, A. I. (2019). Comparison of simple battery model and Thevenin battery model for SOC estimation based on OCV method. In *2019 International Conference on Information and Communications Technology (ICOIACT)* (pp. 738-743). IEEE. https://doi.org/10.1109/ICOIACT46704.2019.8938495

Tremblay, O., & Dessaint, L.-A. (2009). Experimental validation of a battery dynamic model for EV applications. *World Electric Vehicle Journal*, *3*(2), 289-298. https://doi.org/10.3390/wevj3020289

Tuluhong, A., Xu, Z., Chang, Q., & Song, T. (2025). Recent developments in bidirectional DC–DC converter topologies, control strategies, and applications in photovoltaic power generation systems: A comparative review and analysis. *Electronics*, *14*(2), 389. https://doi.org/10.3390/electronics14020389

Wang, J., Wang, B., Zhang, L., Wang, J., Shchurov, N. I., & Malozyomov, B. V. (2022). Review of bidirectional DC–DC converter topologies for hybrid energy storage systems of new energy vehicles. *Green Energy and Intelligent Transportation*, *1*(2), 100010. https://doi.org/10.1016/j.geits.2022.100010

Wang, L., Deng, X., Han, P., Qi, X., Wu, X., Li, M., & Xu, H. (2019). Electromagnetic transient modeling and simulation of power converters based on a piecewise generalized state-space averaging method. *IEEE Access*, *7*, 12241-12251. https://doi.org/10.1109/ACCESS.2019.2892549

Appendix

The Jacobian matrices of the linear model in Equation (24) are as follows:

$$\mathbf{A}(x_0,u_0)=\begin{bmatrix} -\dfrac{K_{pi}}{A_rL}x_{2\_0} & a(1,2) & \dfrac{1}{L} & \dfrac{K_{pi}K_{iv}}{A_rL}x_{2\_0} & \dfrac{K_{ii}}{A_rL}x_{2\_0} \\ a(2,1) & \dfrac{K_{pi}K_{pv}}{A_rC}x_{1\_0}+\dfrac{P_{CPL\_0}}{Cx_{2\_0}^2} & 0 & -\dfrac{K_{pi}K_{iv}}{A_rC}x_{1\_0} & -\dfrac{K_{ii}}{A_rC}x_{1\_0} \\ -\dfrac{1}{C_{Batt}} & 0 & -\dfrac{1}{R_{\text{int}}C_{Batt}} & 0 & 0 \\ 0 & -1 & 0 & 0 & 0 \\ -1 & -K_{pv} & 0 & K_{iv} & 0 \end{bmatrix}_{5\times5}$$

$$a(1,2)=-\frac{1}{L}+\frac{K_{pi}K_{pv}}{A_rL}x_{2\_0}^{*}-\frac{2K_{pi}K_{pv}}{A_rL}x_{2\_0}+\frac{K_{pi}K_{iv}}{A_rL}x_{v\_0}-\frac{K_{pi}}{A_rL}x_{1\_0}+\frac{K_{ii}}{A_rL}x_{i\_0}$$

$$a(2,1)=\frac{1}{C}-\frac{K_{pi}K_{pv}}{A_rC}x_{2\_0}^{*}+\frac{K_{pi}K_{pv}}{A_rC}x_{2\_0}-\frac{K_{pi}K_{iv}}{A_rC}x_{v\_0}-\frac{2K_{pi}}{A_rC}x_{1\_0}+\frac{K_{ii}}{A_rC}x_{i\_0}$$

$$\mathbf{B}(x_0,u_0)=\begin{bmatrix} \dfrac{K_{pi}K_{pv}}{A_rL}x_{2\_0} & 0 & 0 \\ -\dfrac{K_{pi}K_{pv}}{A_rC}x_{1\_0} & -\dfrac{1}{Cx_{2\_0}} & 0 \\ 0 & 0 & \dfrac{1}{R_{\text{int}}C_{Batt}} \\ 1 & 0 & 0 \\ K_{pv} & 0 & 0 \end{bmatrix}_{5\times3}$$

$$\mathbf{C}(x_0,u_0)=\begin{bmatrix} 1 & 0 & 0 & 0 & 0 \\ 0 & 1 & 0 & 0 & 0 \\ 0 & 0 & 1 & 0 & 0 \end{bmatrix}_{3\times5}$$

$$\mathbf{D}(x_0,u_0)=\begin{bmatrix} 0 & 0 & 0 \\ 0 & 0 & 0 \\ 0 & 0 & 0 \end{bmatrix}_{3\times3}$$